Applied Surface Science 369 (2016) 1–10

Contents lists available at ScienceDirect

Applied Surface Science

journal homepage: www.elsevier.com/locate/apsusc

Novel multifunctional $NiFe_2O_4$/ZnO hybrids for dye removal by adsorption, photocatalysis and magnetic separation

Hua-Yue Zhu [a,b], Ru Jiang [a,b,*], Yong-Qian Fu [a], Rong-Rong Li [c], Jun Yao [a,b], Sheng-Tao Jiang [a,b]

[a] Zhejiang Provincial Key Laboratory of Plant Evolutionary Ecology and Conservation, Taizhou University, Taizhou, Zhejiang 318000, PR China
[b] Department of Environmental Engineering, Taizhou University, Taizhou, Zhejiang 318000, PR China
[c] College of Pharmaceutical and Chemical Engineering, Taizhou University, Taizhou, Zhejiang 318000, PR China

ARTICLE INFO

Article history:
Received 31 December 2015
Received in revised form 1 February 2016
Accepted 4 February 2016

Keywords:
Photocatalysis
Adsorption
Congo red
Magnetic separation
$NiFe_2O_4$/ZnO hybrids

ABSTRACT

Novel multifunctional $NiFe_2O_4$/ZnO hybrids were prepared by a hydrothermal method and their physicochemical properties were characterized by XRD, SEM, TEM, TGA, VSM, BET and UV–vis DRS. The adsorption and photocatalytic performance of $NiFe_2O_4$/ZnO hybrids were systematically investigated using congo red as a model contaminant. With the introduction of $NiFe_2O_4$, $NiFe_2O_4$/ZnO hybrids can absorb the whole light from 300 nm to 700 nm. The adsorption capacity (221.73 mg g^{-1}) of $NiFe_2O_4$/ZnO hybrids is higher than those of $NiFe_2O_4$, ZnO and mechanically mixed $NiFe_2O_4$/ZnO hybrids. The removal of congo red solution (20 mg L^{-1}) by $NiFe_2O_4$/ZnO hybrids was about 94.55% under simulated solar light irradiation for 10 min. $^{\bullet}$OH and h^+ play important roles in the decolorization of congo red solution by $NiFe_2O_4$/ZnO hybrids under simulated solar light irradiation. The decolorization efficiency of congo red solution is 97.23% for the fifth time by $NiFe_2O_4$/ZnO hybrids under simulate solar light irradiation, indicating the high photostability and durability. NO_3^- and Cl^- anions which are ubiquitous components in dye-containing wastewater have negligible influence on the effectiveness of $NiFe_2O_4$/ZnO hybrids. Moreover, the magnetic $NiFe_2O_4$/ZnO hybrids can be easily separated from the reacted solution by an external magnet.

1. Introduction

Heterogeneous photocatalysis using novel functional materials could provide efficient and important technologies for treatment of organic wastewater [1–8]. Over the last decade, ZnO with a wide band gap (E_g = 3.37 eV) is one of the most important photocatalysts, which has been widely used in photocatalytic degradation of organic pollutants [9–15]. However, for the actual applications, traditional ZnO photocatalysts are usually not suitable due to the inconvenient and expensive separation [16], serious photocorrosion [17], and low quantum efficiency resulted from its disadvantages of wide bandgap and the rapid recombination of photo-generated carriers [11,17,18].

In order to decrease photocorrosion and enhance further the photostability, much efforts have been made by developing novel efficient and stable ZnO-based photocatalysts such as CdS/ZnO [19], SnO_2/ZnO [20], ZnO/graphene oxide [18], TiO_2/ZnO [21]. Although those ZnO-based photocatalysts are efficient and photostable, the difficulty in separating from aqueous solutions limits their practical application in dye-containing organic wastewater treatment [16,18,21]. To solve the above problem, a convenient and viable strategy to integrate nanomaterials with strong magnetic component such as Fe_3O_4 [13,22,23], γ-Fe_2O_3 [24], $ZnFe_2O_4$ [25,26], $NiFe_2O_4$ [27], and $CoFe_2O_4$ [2,28], was applied to prepare magnetic nanomaterials that can be separated by applying an external magnetic field. Among all kinds of magnetic components, $NiFe_2O_4$ nanoparticles are one of the most useful contenders due to its moderate saturation magnetization [29,30], strong catalytic property [27,31], photo-chemical stability [32], and high adsorption capacity [33,34]. In addition, $NiFe_2O_4$ nanoparticles have high performance for photodegrading aqueous dyes and can be separated easily using an external magnet [27,32,35]. If magnetic $NiFe_2O_4$ nanoparticles are coupled with ZnO nanoparticles, it is possible to improve the efficiency of charge separation and decrease photocorrosion of ZnO itself, leading to high photocatalytic performance and convenient separation. Although $NiFe_2O_4$/ZnO hybrids were obtained under ultrasonic irradiation [36], study on preparation, characterization

* Corresponding author at: No. 1139, Municipal Government Avenue, Taizhou, Zhejiang 318000, PR China.
E-mail address: jiangru0576@163.com (R. Jiang).

http://dx.doi.org/10.1016/j.apsusc.2016.02.025
0169-4332/© 2016 Published by Elsevier B.V.

and adsorption-photocatalytic properties of novel multifunctional $NiFe_2O_4$/ZnO hybrids for fast and highly efficient removal of organic pollutants from aqueous solution have not yet been reported.

In this study, novel multifunctional $NiFe_2O_4$/ZnO hybrids were prepared by a hydrothermal method and have been characterized by XRD, SEM, TEM, TGA, VSM, BET and UV–vis DRS. The adsorption and photocatalytic performance of $NiFe_2O_4$/ZnO hybrids were systematically investigated using congo red (CR) as a model contaminant. The effect of ubiquitous anions on the photocatalytic activity of $NiFe_2O_4$/ZnO hybrids was studied in detail. Besides, the stability and reusability of $NiFe_2O_4$/ZnO hybrids was also examined. This study could greatly promote the potential applications of magnetic ZnO-based photocatalysts in eliminating hazardous contaminants.

2. Materials and methods

2.1. Materials

Congo red (CR) was purchased from Yongjia Fine Chemical Factory (Wenzhou, China). Zinc oxide (Purity > 99.0%) were supplied by Wanjiang New Materials Co., Ltd (Hangzhou, China). $NiSO_4{\cdot}6H_2O$, $FeCl_3{\cdot}6H_2O$, edetate disodium salt (EDTA-2Na), t-butyl alcohol (TBA), sodium hydroxide (99%) and other reagents of analytical grade were purchased from Shanghai Chemical Reagents Research Institute (Shanghai, China) and were used without further purification.

2.2. Preparation of $NiFe_2O_4$/ZnO hybrids

$NiFe_2O_4$/ZnO hybrids were synthesized using a hydrothermal method as follows: $FeCl_3{\cdot}6H_2O$ (1.00 g) and $NiSO_4{\cdot}6H_2O$ (0.56 g) were dissolved into 25 mL of distilled water to obtain brown-green solution. ZnO (1.33 g) was dispersed in 60 mL of distilled water by ultrasonic treatment for 60 min. Subsequently, the two systems were mixed by ultrasonic treatment. NaOH solution (6 mol L^{-1}) was added dropwise to the suspended system until its pH around 13. The reacted system was further stirred for 1 h, and then brown suspended system was transferred into an autoclave in an oven and kept at 180 °C for 20 h. The brown-gray precipitate was separated by an external magnet, washed with distillated water and dried in an oven at 110 °C till constant weight. The weight ratio of $NiFe_2O_4$ and ZnO in $NiFe_2O_4$/ZnO hybrids is about 1:2.

The corresponding $NiFe_2O_4$ nanoparticles were also facilely synthesized using the same method but in the absence of ZnO nanoparticles. The weight of $NiFe_2O_4$ nanoparticles obtained was about 0.665 g. The prepared $NiFe_2O_4$ nanoparticles and commercial ZnO nanoparticles in a 1:2 of weight ratio mixed directly and pulverized to obtain mechanically mixed $NiFe_2O_4$/ZnO hybrids (m-$NiFe_2O_4$/ZnO) for comparison.

2.3. Characterization of materials

The XRD patterns of $NiFe_2O_4$/ZnO hybrids were recorded on a Bruker AXS D8-advance X-ray diffractmeter, using Kα radiation (λ=0.154 nm). The Brunauer–Emmett–Teller (BET) specific surface area, average pore diameter, pore volume, and isotherms were measured was obtained using a MPMS-XL-7 surface area and porosity analyzer (Quantum Design, America). The morphologies of the materials were characterized with a scanning electron microscopy (SEM, Hitachi S480). Transmission electron microscopy (TEM) and high resolution Transmission electron microscopy (HRTEM) were performed on a FEI Tecnai G20 with a field emission gun at 200 kV. The UV–vis diffuse reflectance spectra were obtained by using an UV-3100 UV-vis spectrophotometer (Hitachi Corporation, Japan). VSM measurements were performed by using a MPM5-XL-5 superconducting quantum interference device (SQUID) magnetometer in an external field up to 6.5. Thermogravimetric analyses (TGA) and differential scanning calorimetry (DSC) of samples were performed in a Setaram Setsys 16 TG/DTA/DSC (France) from 17 °C to 800 °C with a heating rate of 2 °C min^{-1}.

2.4. Isotherm experiments

Isotherm experiments were conducted with a constant dosage (1.0 g L^{-1}) and varying initial concentrations of CR in the range 50–1000 mg L^{-1} using a model KYC-1102 air-temperature-controlled shaker (Ningbo Jiangnan Instrument Factory, China) at 100 rpm. Typically, a 50 mL solution of known dye concentrations and 0.05 g of $NiFe_2O_4$/ZnO hybrids were added into 100 mL flasks and then shook under 25 ± 0.2 °C. At given time intervals, 2 mL of the suspensions were collected and $NiFe_2O_4$/ZnO hybrids were separated from aqueous solution using a magnet. The concentrations of the residual CR were analyzed by a TU 1810 UV-visible spectrophotometer (Beijing Purkinje General Instrument Co., Ltd, China). The amount of CR adsorbed on $NiFe_2O_4$/ZnO hybrids, q_t, was obtained as follows:

$$q_t = \frac{(C_0 - C_t) \times V}{m} \tag{1}$$

where C_0 and C_t are the initial CR concentration and instant CR concentration at any time t (mg L^{-1}), respectively, V is the volume of solution (L) and m is the amount of adsorbent (g).

2.5. Photocatalytic experiments

The photocatalytic activities of materials were evaluated by photocatalytic decolorization of CR solution under simulated solar light irradiation. The reaction system includes a 350 W Xe arc lamp, some quartz reactors (50 mL of internal volume), a water cooling system, etc. In this study, adsorption and photocatalysis of CR solution by $NiFe_2O_4$/ZnO hybrids were carried out simultaneously. In a typical experiment, 0.05 g photocatalyst was added into 50 mL of CR solution (20 mg L^{-1}) to start immediately the reaction under simulated solar light irradiation. Initial pH value of CR dye solution (20 mg L^{-1}) is about 5.6. To ensure effective mixing of $NiFe_2O_4$/ZnO hybrids and CR solution and keep constant concentration of dissolved oxygen, the reaction solution was agitated by bubbling air continuously during the whole reaction. After irradiating for regular periods of time, aliquots (about 2.0 mL) were drawn and the photocatalyst was separated by an external magnet. Residual CR concentrations were analyzed by measuring the absorbance peak at 496 nm in a TU 1810 UV-visible spectrophotometer (Beijing Purkinje General Instrument Co., Ltd, China). The decolorization efficiency η (%) of CR solution can be calculated according to Eq. (2).

$$\eta(\%) = \frac{(C_0 - C_t)}{C_0} \times 100 \tag{2}$$

where C_0 is the initial concentration of CR in the solution (mg L^{-1}), C_t is the concentration of CR at time t (mg L^{-1}).

According to previous studies [21], photocatalytic reactions kinetics can be expressed by the Langmuir–Hinshelwood (L-H) model. When initial concentration of pollutant is lower, the reaction rate of L-H model can be expressed as:

$$\ln\left(\frac{C_0}{C_t}\right) = k_{app}t \tag{3}$$

where k_{app} is the apparent reaction rate constant (min^{-1}). A plot of $\ln(C_0/C_t)$ versus t will yield a slope of k_{app}.

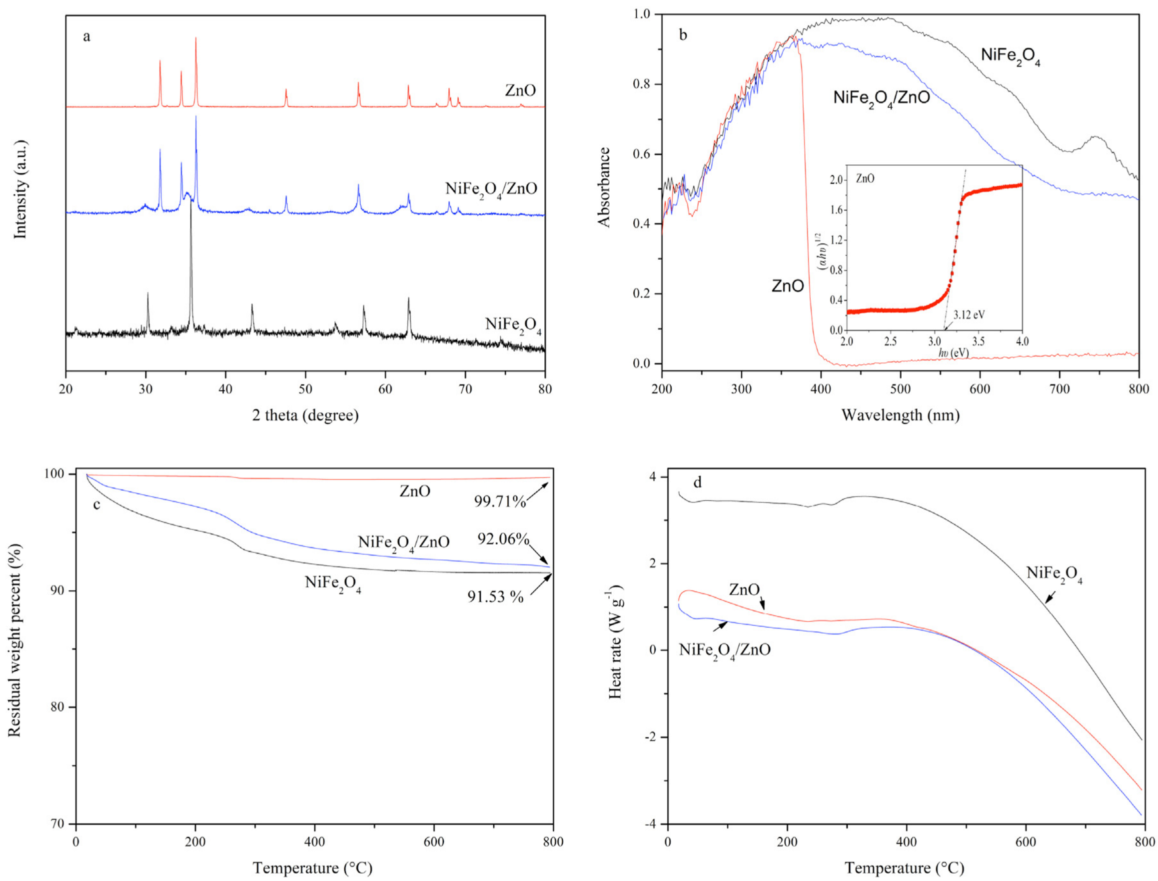

Fig. 1. XRD (a), UV–vis DRS (b), TGA (c) and DSC (d) curves of ZnO, $NiFe_2O_4$ and $NiFe_2O_4$/ZnO hybrids.

3. Results and discussions

3.1. Characterization of samples

The crystal structures of the as-prepared samples were analyzed with XRD and the results are shown in Fig. 1a. The XRD pattern of ZnO shows obvious peaks for hexagonal zinc oxide (JCPDS no. 79-0206). The most intense of ZnO were at 2θ of 31.78°, 34.35°, 36.26°, 47.56°, 56.60°, 62.86°, 67.96° and 69.16°, which are corresponded to the (100), (002), (101), (102), (110), (103), and (112) and (201) planes, respectively [15]. All the diffraction peaks of $NiFe_2O_4$ at the 2θ values of 30.26°, 35.64°, 43.30°, 53.83°, 57.26°, and 62.89° are indexed to (220), (311), (400), (422), (511) and (440) crystal planes of spinel $NiFe_2O_4$ (JCPDS no. 54-0964), respectively [27,35]. For $NiFe_2O_4$/ZnO hybrids, the (100), (002), (101), (102), (110), (103), (112) and (201) peaks belong to hexagonal ZnO phase while the (220), (311), and (400) peaks correspond to spinel $NiFe_2O_4$ phase. Comparatively, no obvious other peaks of impurity are observed except for the peaks of both ZnO and $NiFe_2O_4$ and a weak peak of $NiFe_2O_4$ at the 2θ values of 53.83° (511) disappeared in $NiFe_2O_4$/ZnO hybrids.

UV–vis diffuse reflectance spectroscopy was used in order to determine the light absorbance performances of $NiFe_2O_4$, ZnO and $NiFe_2O_4$/ZnO hybrids, as shown in Fig. 1b. It displays that pure ZnO has an optical-absorption edge at about 386 nm, indicating that the pure ZnO absorb only UV light. $NiFe_2O_4$ nanoparticles absorb the light in the whole region ranging from 300 to 700 nm, which is consistent with the previous observation [27]. While the light absorbance curve of $NiFe_2O_4$/ZnO hybrids is much closer to that of pure $NiFe_2O_4$, which is in agreement with the dark color of the sample. There is an obvious broad absorbance in the visible light region for $NiFe_2O_4$/ZnO hybrids, implying that the coupling structure of $NiFe_2O_4$/ZnO hybrids may provide efficient visible-light sensitive photocatalysis. By calculating from the plots $(\alpha h\upsilon)^{1/2}$ vs. photo energy ($h\upsilon$), the approximate E_g value of ZnO is about ~3.12 eV [9,28], as presented in the inset of Fig. 1b, while ~1.60 eV and ~1.71 eV for $NiFe_2O_4$ and $NiFe_2O_4$/ZnO hybrids, respectively [29]. Therefore, the addition of $NiFe_2O_4$ is an advisable way to enhance the optical absorption property of ZnO nanoparticle.

TGA curves and DSC curves of $NiFe_2O_4$, ZnO and $NiFe_2O_4$/ZnO hybrids are shown in Fig. 1c and d. As shown in Fig. 1c, ZnO is considerably stable in the whole process, which is attributed to the desorption of water adsorbed on the surface of ZnO nanoparticles over a temperature range of 220–280 °C [37]. Above 280 °C, the weight loss of ZnO is almost negligible. The TGA–DSC curves of $NiFe_2O_4$/ZnO hybrids behave similarly to those of $NiFe_2O_4$. From the TGA curves of $NiFe_2O_4$ and $NiFe_2O_4$/ZnO hybrids, it could be seen that both samples exhibits two distinctive weight loss stages in the TGA curves. The first stage took place in the temperature range of 17–160 °C due to the evaporation of adsorbed water. The second weight loss step occurred in the temperature range of 160–400 °C. The overall weight loss is 0.29%, 8.47% and 7.94% for ZnO, $NiFe_2O_4$ and $NiFe_2O_4$/ZnO hybrids, respectively. Compared with ZnO, there are more weight losses in $NiFe_2O_4$ and $NiFe_2O_4$/ZnO hybrids because of the strong interactions between the d orbitals of the surface Fe atom and the adsorbing OH radical molecular orbitals [38]. Since there is not any distinct exothermal or endothermic peak found in the corresponding DSC curves over the temperature range of 17–800 °C (Fig. 1d), which implies no any phase transition for all three materials lower than 800 °C [39]. As a result, $NiFe_2O_4$, ZnO and $NiFe_2O_4$/ZnO hybrids are quite thermo-stable under high temperatures lower than 800 °C.

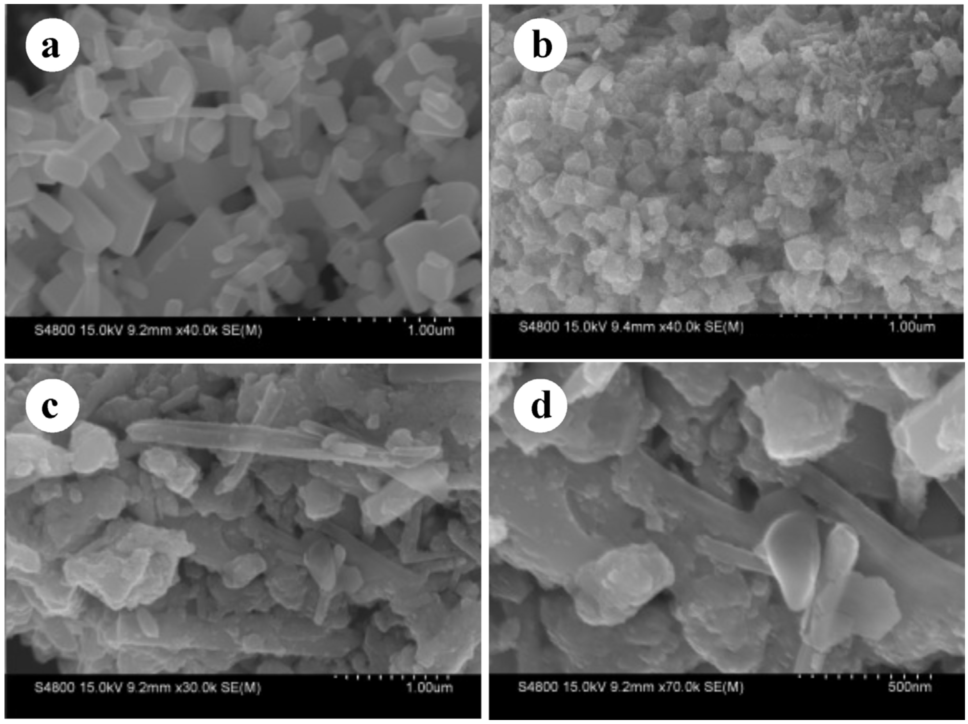

Fig. 2. SEM images of ZnO (a), $NiFe_2O_4$ (b) and $NiFe_2O_4$/ZnO hybrids (c, d).

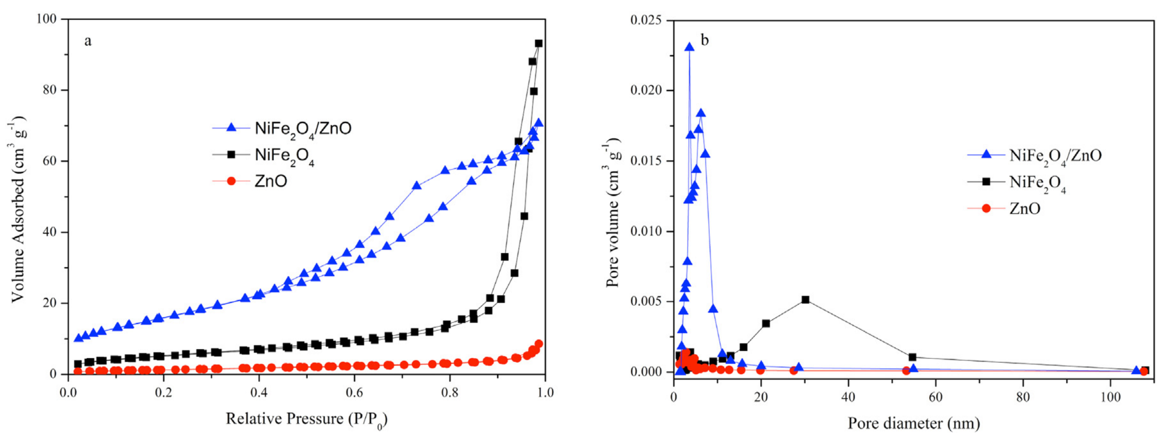

Fig. 3. Nitrogen adsorption–desorption isotherms (a) and pore size distribution curves (b) of $NiFe_2O_4$, ZnO and $NiFe_2O_4$/ZnO hybrids.

The morphologies of ZnO, $NiFe_2O_4$, and $NiFe_2O_4$/ZnO hybrids were studied by SEM. ZnO nanoparticles with a mean diameter of 32 nm are present and the surface of ZnO nanoparticles is very smooth (Fig. 2a). It is clearly illustrated that the pure $NiFe_2O_4$ sample is constructed with lots of nanoparticles with a diameter of 70–200 nm (Fig. 2b). The obvious aggregation of pure $NiFe_2O_4$ sample may be attributed to the small size effect and the surface effect. Comparing the morphology of $NiFe_2O_4$/ZnO hybrids with that of ZnO, it clearly suggests that the introduction of $NiFe_2O_4$ is of great importance for obtaining a porous structure of the novel materials (Fig. 2c and d).

The N_2 adsorption–desorption isotherms were used to investigate the BET specific surface area and porous structure of the as-prepared ZnO, $NiFe_2O_4$ and $NiFe_2O_4$/ZnO hybrids (Fig. 3). According to the IUPAC classification, the isotherms of $NiFe_2O_4$ and $NiFe_2O_4$/ZnO hybrids are of type IV with a narrow hysteresis loops, indicating the mesoporous structure of $NiFe_2O_4$ and $NiFe_2O_4$/ZnO hybrids (Fig. 3a). However, the isotherm of ZnO is type II because of the monolayer formation of ZnO [40]. The specific surface area values (S_{BET}), average pore diameter size (d) and pore volume (V_g) are reported in Table 1. The BET specific surface area of ZnO, $NiFe_2O_4$ and $NiFe_2O_4$/ZnO hybrids is 4.73 $m^2\ g^{-1}$, 19.02 $m^2\ g^{-1}$ and 59.89 $m^2\ g^{-1}$, respectively (Table 1). The Fig. 3b shows the pore size distribution plots calculated using the BJH equation from the desorption branch of the isotherm. The pore size distribution measurements indicate that the $NiFe_2O_4$/ZnO hybrids have pronounced mesoporosity of narrow pore size distribution with average pore diameter around 7.30 nm. Compared with $NiFe_2O_4$, $NiFe_2O_4$/ZnO

Table 1
Pore structural parameters of $NiFe_2O_4$, ZnO and $NiFe_2O_4$/ZnO hybrids.

Materials	SBET ($m^2\ g^{-1}$)	d (nm)	V_g ($cm^3\ g^{-1}$)
$NiFe_2O_4$/ZnO	59.89	7.30	0.109
ZnO	4.73	11.24	0.014
$NiFe_2O_4$	19.02	30.30	0.144

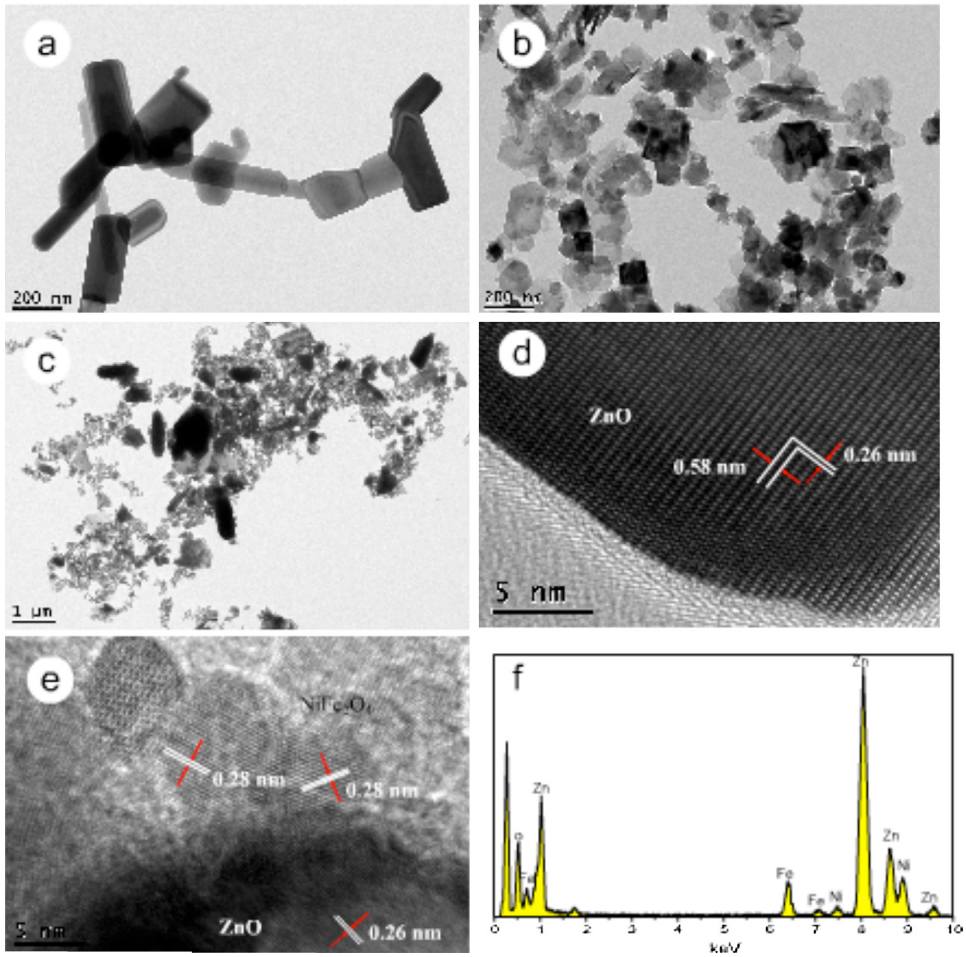

Fig. 4. TEM images of pure ZnO (a), $NiFe_2O_4$ (b), $NiFe_2O_4$/ZnO hybrids (c), HRTEM images of ZnO (d), $NiFe_2O_4$/ZnO hybrids (e), and EDS of $NiFe_2O_4$/ZnO hybrids (f).

hybrids have a narrower pore size distribution and smaller pore diameter, which results from the close coupling by interactions between $NiFe_2O_4$ and ZnO nanoparticles in $NiFe_2O_4$/ZnO hybrids (Fig. 2d). As a result, $NiFe_2O_4$/ZnO hybrids can provide more active sites and adsorb more reactive species due to narrower pore size distribution and larger BET surface area [35].

To further confirm the structure of ZnO, $NiFe_2O_4$ and $NiFe_2O_4$/ZnO hybrids, TEM analysis was carried out. As seen in Fig. 4a, it shows the hexagonal morphology of ZnO nanoparticles in the range of 20–350 nm. From TEM image, it is observed that the $NiFe_2O_4$ nanoparticles are irregular structure in nature. The average particle size determined from the TEM micrographs is around 103 nm (Fig. 4b). Fig. 4c shows the TEM image of the $NiFe_2O_4$/ZnO hybrids. $NiFe_2O_4$ nanoparticles are located on the surface of the dark dots. Compared with sole $NiFe_2O_4$ (Fig. 4b), the size of $NiFe_2O_4$ nanoparticles are decreased from 103 nm to 11 nm, which indicates that the presence of hexagonal ZnO nanoparticles inhibited the growth of $NiFe_2O_4$ particles in this composite system. In addition, the pore size of $NiFe_2O_4$/ZnO hybrids has a smaller size than that of $NiFe_2O_4$, indicating that the presence of ZnO plays significant effect not only on the average particle size but also on the pore size. The corresponding high-magnification TEM images of hexagonal ZnO (Fig. 4d) and the $NiFe_2O_4$/ZnO hybrids (Fig. 4e) show clearly the crystalline lattice fringes. HRTEM image of ZnO shows clear lattice fringes (0.260 nm), which represents the (002) planes of the hexagonal ZnO (Fig. 4d). The clear atomic lattice fringe (about 0.28 nm) is close to the (211) lattice planes of $NiFe_2O_4$ crystal (Fig. 4e) [31]. $NiFe_2O_4$ are tightly coupled on the surface of ZnO (Fig. 4e), which is favorable for the charge transfer between $NiFe_2O_4$ and ZnO and enhances the separation of photogenerated electron–hole pairs and subsequently photocatalytic performance [41]. In order to obtain more detailed contents information of the $NiFe_2O_4$/ZnO hybrids, EDS spectra from the Fig. 4f gives the signals of Zn, O, Ni, and Fe elements in the composites.

Moreover, the magnetic properties of $NiFe_2O_4$ and $NiFe_2O_4$/ZnO hybrids were studied and the magnetic hysteresis loops are depicted in Fig. 5. The $NiFe_2O_4$ exhibits a typical ferromagnetic behavior at room temperature, and the saturation magnetization (Ms) is about 35.53 emu g^{-1}. This difference between experimental Ms value and theoretical Ms value (50 emu g^{-1}) of $NiFe_2O_4$ calculated using Neel's sublattice theory can be attributed to the finite size effects [30]. It was note worthy that value (11.72 emu g^{-1}) of $NiFe_2O_4$/ZnO hybrids is much lower than that of the $NiFe_2O_4$, which is ascribed to the existence of nonmagnetic ZnO in the total mass. However, the Ms value of $NiFe_2O_4$/ZnO hybrids is still much higher than those of reported magnetic photocatalysts and ensures better magnetic response of $NiFe_2O_4$/ZnO hybrids toward an external magnetic field [42–44]. The $NiFe_2O_4$/ZnO hybrids can be completely attracted and separated from the treated solution by applying an external magnetic field within 20 s (inset in Fig. 5). Therefore, excellent magnetically separation of $NiFe_2O_4$/ZnO hybrids is advantage and positive for eliminating organic pollutants and economic treatment of industrial wastewater.

3.2. Adsorption of CR on $NiFe_2O_4$/ZnO hybrids

During the photocatalysis, the excellent adsorption is contributed to the improvement of photocatalytic activity. Prior to the photocatalytic removal under simulated solar light irradiation, the dark adsorption of CR on different materials was evaluated and the corresponding adsorption isotherms were recorded. In this study, Langmuir (Eq. (4)) and Freundlich (Eq. (5)) isotherm models were used to describe the equilibrium adsorption for CR dye on four materials [45,46].

$$\frac{c_e}{q_e} = \frac{1}{bq_m} + \frac{c_e}{q_m} \tag{4}$$

$$\ln\ q_e = \ln K_F + \frac{1}{n}\ln\ c_e \tag{5}$$

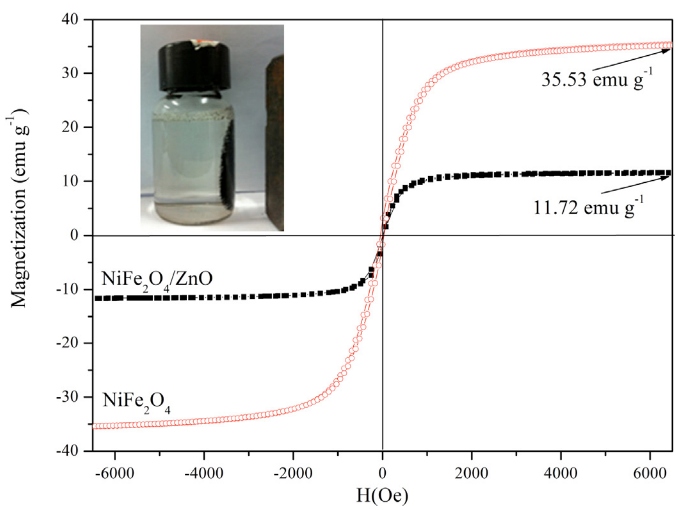

Fig. 5. Room-temperature magnetic hysteresis loops for $NiFe_2O_4$ and $NiFe_2O_4$/ZnO hybrids (inset: the magnetic separation of $NiFe_2O_4$/ZnO hybrids by a magnet).

where C_e (mg L^{-1}) is equilibrium concentration of CR in solution, q_e (mg g^{-1}) is adsorption capacity of CR adsorbed on adsorbent at equilibrium, q_m (mg g^{-1}) is maximum amounts of CR adsorbed per unit mass of adsorbent required for monolayer coverage of the surface, b (L mg^{-1}) is a Langmuir constant related to the heat of adsorption. The slope and intercept of linear plots of c_e/q_e against c_e yield the values of $1/q_m$ and $1/bq_m$ for Eq. (4). K_F (mg$^{1-(1/n)}$ L$^{1/n}$ g^{-1}) is related to the adsorption capacity of the adsorbent and $1/n$ is another constant related to the surface heterogeneity. The slope and intercept of linear plots of $\ln q_e$ against $\ln c_e$ yield the values of $1/n$ and $\ln K_F$ for Eq. (5).

The equilibrium adsorption experimental data of CR by $NiFe_2O_4$/ZnO hybrids, ZnO, $NiFe_2O_4$, and m-$NiFe_2O_4$/ZnO hybrids are presented in Fig. 6a. The adsorption capacities of CR on four materials increase rapidly in lower concentration range of 5–1000 mg L^{-1} while the saturation of CR adsorption is obtained at equilibrium value C_e of 600 mg g^{-1} (Fig. 6a). The theoretical parameters (q_m, b, K_F, n, and R^2) of adsorption isotherms are summarized in Table 2. As seen from Table 2, the fitting correlation coefficient (R^2) from the Langmuir model are all higher than 0.994 and the calculated values of q_m obtained from Langmuir isotherm model are consistent with those experimentally obtained, indicating that the Langmuir model adequately describes the CR adsorption on all four materials. The linearized Langmuir plots are given in Fig. 6b. The result indicates that there are homogeneous distributions of active sites onto four materials since the Langmuir model assumes that the surface is homogenous [46]. The maximum adsorption capacity of CR on $NiFe_2O_4$/ZnO hybrids, ZnO, $NiFe_2O_4$, and m-$NiFe_2O_4$/ZnO hybrids estimated by the Langmuir adsorption isotherm model was 221.73 mg g^{-1}, 19.88 mg g^{-1}, 47.33 mg g^{-1}, and 28.29 mg g^{-1}, respectively. Usually, the adsorption capacities of materials for dye removal are mainly dependent on surface properties and functional groups of adsorbent. Indeed, $NiFe_2O_4$ are well known for their high adsorption properties of organic dyes [34] and bovine serum albumin [33] because of its large BET specific surface area and abundant surface functional groups, such as HOH, Fe-OH [47]. As shown in Table 1, what's more, $NiFe_2O_4$/ZnO hybrids are of a

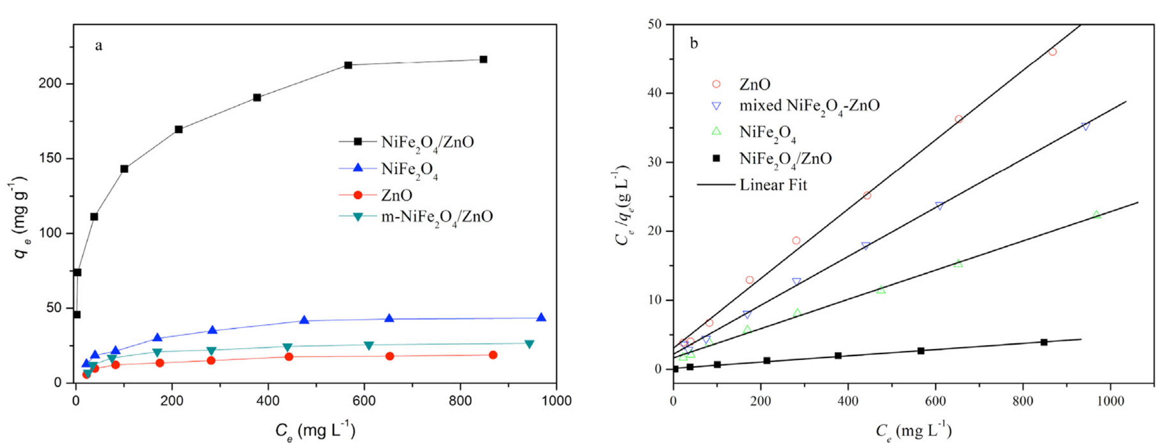

Fig. 6. (a) CR adsorption isotherms and (b) Langmuir adsorption isotherms over $NiFe_2O_4$, ZnO, $NiFe_2O_4$/ZnO hybrids and m-$NiFe_2O_4$/ZnO.

Table 2
Adsorption isotherm constants for CR adsorption on different materials.

Materials	$q_{e,exp}$ (mg g^{-1})	Langmuir isotherm constants			Freundlich isotherm constants		
		q_m (mg g^{-1})	b	R^2	K_F (mg$^{1-(1/n)}$ L$^{1/n}$ g^{-1})	n	R^2
$NiFe_2O_4$/ZnO	216.53	221.73	0.0288	0.994	0.036	4.23	0.978
ZnO	18.84	19.88	0.0163	0.997	0.397	4.78	0.989
$NiFe_2O_4$,	43.49	47.33	0.0126	0.997	0.544	1.49	0.982
m-$NiFe_2O_4$/ZnO	26.71	28.29	0.0160	0.999	0.409	1.47	0.964

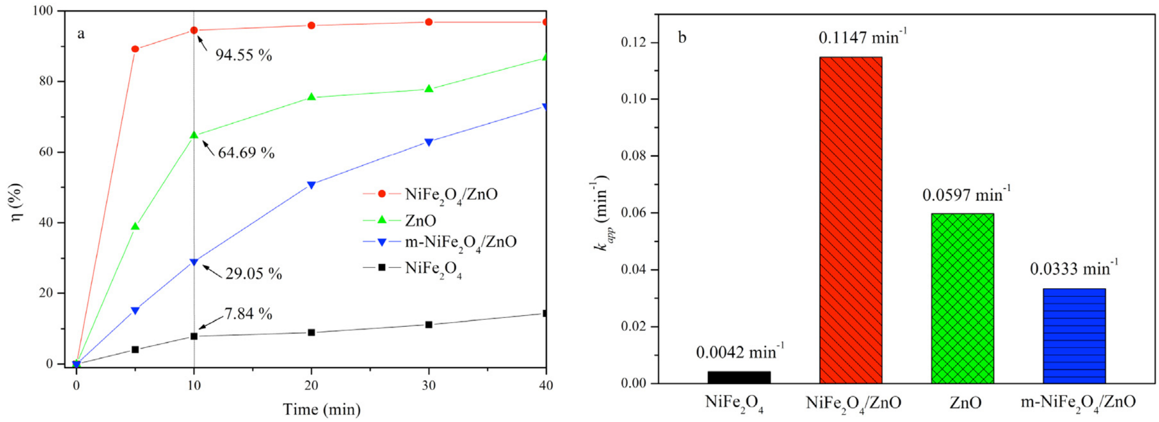

Fig. 7. (a) Photodecolorization of CR as a function of the irradiation time and (b) the reaction rate constant over $NiFe_2O_4$, ZnO, $NiFe_2O_4$/ZnO and m-$NiFe_2O_4$/ZnO hybrids (initial CR concentration: 20 mg L^{-1}; dosage: 1.0 g L^{-1}; natural pH).

large surface area (59.89 m^2 g^{-1}), much higher than those of the referenced $NiFe_2O_4$ (19.02 m^2 g^{-1}), and hence exhibits significantly enhanced adsorption to CR dye.

The validity of the Langmuir adsorption process is assessed by a dimensionless constant separation factor R_L, as equation Eq. (6).

$$R_L = \frac{1}{1 + C_0 b} \tag{6}$$

where C_0 (mg L^{-l}) is initial CR concentration of CR in solution, b (L mg^{-1}) is a Langmuir constant, which can be calculated from Eq. (5).

Usually, the value of R_L indicates whether the isotherm is unfavorable ($R_L > 1$), linear ($R_L = 1$), favorable ($0 < R_L < 1$), or irreversible ($R_L = 0$). For CR adsorption on $NiFe_2O_4$/ZnO hybrids, the R_L values calculated from Eq. (5) are found to be between 0.874 and 0.033 for the initial CR concentrations in the range 5–800 mg L^{-1}, indicating that the adsorption of CR on $NiFe_2O_4$/ZnO hybrids is favorable and reversible irrespective.

A comparison of the maximum CR adsorption capacity (q_m value) of $NiFe_2O_4$/ZnO hybrids with those of other materials in the literatures is shown in Table 3. It can be seen from the Table 3 that $NiFe_2O_4$/ZnO hybrids show the comparable adsorption capacity with respect to ZnO, $NiFe_2O_4$, and m-$NiFe_2O_4$/ZnO hybrids in this study. In addition, the adsorption capacity of $NiFe_2O_4$/ZnO hybrids was higher than those of metal oxide adsorbents reported such as NiO nanoparticles [48], NiO nanosheets [48], $Fe_{3-x}La_xO_4$ [49], γ-Fe_2O_3 [50], and MFe_2O_4 (M = Mn, Fe, Co, Ni) [51,52]. Therefore, $NiFe_2O_4$/ZnO hybrids is suitable and promising material for CR removal from aqueous solutions since it has a relatively high adsorption capacity and is easily recovered from effluents by applying an external magnet.

Table 3
The q_m values for the adsorption of CR on different adsorbents.

Materials	q_m (mg g^{-1})	Ref.
$NiFe_2O_4$/ZnO	221.73	This study
ZnO	19.88	This study
$NiFe_2O_4$,	47.33	This study
m-$NiFe_2O_4$/ZnO	28.29	This study
NiO nanoparticles	39.7	[48]
NiO nanosheets	151.7	[48]
$Fe_{3-x}La_xO_4$	37.4–79.1	[49]
γ-Fe_2O_3	208.33	[50]
Zn-Fe_2O_4	16.58	[51]
$MnFe_3O_4$	92.4	[52]
$NiFe_2O_4$	97.1	[52]

3.3. Photocatalytic decolorization of CR by $NiFe_2O_4$/ZnO hybrids

The photocatalytic activities of four materials have been evaluated through the CR decolorization under simulated solar light irradiation and the corresponding results are shown in Fig. 7. The decolorization efficiency η (%) of CR solution by $NiFe_2O_4$/ZnO hybrids, ZnO, m-$NiFe_2O_4$/ZnO, and $NiFe_2O_4$ under simulated solar light irradiation for 10 min is 94.55%, 64.69%, 29.05% and 7.84%, respectively (Fig. 7a). As shown in Fig. 7b, the initial reaction rate constant k_{app} for the photocatalytic decolorization of CR solution with $NiFe_2O_4$/ZnO hybrids, ZnO, m-$NiFe_2O_4$/ZnO, $NiFe_2O_4$ is 0.1147, 0.0597, 0.0333 and 0.0042 min^{-1}, respectively. Obviously, the decolorization of CR solution by the $NiFe_2O_4$/ZnO dramatically improves compared with those of the other three materials. The photocatalytic activity of four materials increases in the order of $NiFe_2O_4$/ZnO > ZnO > m-$NiFe_2O_4$/ZnO > $NiFe_2O_4$. ZnO removes aqueous CR solution under simulated solar light irradiation at a much faster rate than $NiFe_2O_4$, which indicates the more excellent photocatalytic efficiency than $NiFe_2O_4$. In the presence of $NiFe_2O_4$/ZnO hybrids, CR solution can be decolorized 94.55% after 10 min reaction time. However, at the same period of time, CR decolorization is only 29.05% by m-$NiFe_2O_4$/ZnO. The photoreactivity of m-$NiFe_2O_4$/ZnO is much lower than that of $NiFe_2O_4$/ZnO (rate constant: 0.0333 min^{-1} vs. 0.1147 min^{-1}), indicating that the close interphase contact coupling of $NiFe_2O_4$ and ZnO nanoparticles in $NiFe_2O_4$/ZnO hybrids should play an important role in enhancing the photoreactivity [16]. In general, the close coupling of $NiFe_2O_4$/ZnO hybrids results in enhancing the electron transfer rate between interfaces and hindering the recombination of photo-generated electrons and holes [16].

The active species involved in the photocatalytic degradation reaction are hydroxyl radicals ($^{\bullet}OH$), photogenerated holes (h^+), and superoxide radical anions ($O_2^{\bullet-}$). To better reveal the photocatalytic mechanism, the trapping experiments of reactive species were also performed. T-butyl alcohol (TBA) and disodium ethylenediaminetetraacetate (EDTA-2Na) were employed as a $^{\bullet}OH$ radical scavenger and a hole scavenger, respectively [18]. As shown in Fig. 8, in the absence of TBA and EDTA-2Na, the decolorization efficiency of CR solutions is 89.42% by $NiFe_2O_4$/ZnO hybrids under simulated solar light irradiation for 5 min. However, after adding the hole h^+ scavenger (EDTA-2Na) and $^{\bullet}OH$ radical scavenger (TBA), the decolorization efficiency is significantly suppressed by 21.91% and 53.35% with 5 min irradiation, respectively. Therefore, $^{\bullet}OH$ and h^+ play important roles in the decolorization of CR solution by $NiFe_2O_4$/ZnO hybrids under simulated solar light irradiation.

Based on the above experimental result and some earlier reports on the photocatalytic degradation of organic pollutants [16,27], a

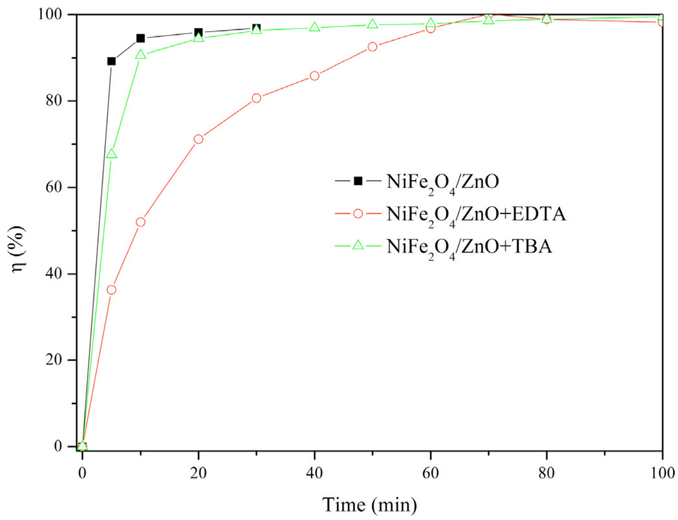

Fig. 8. Effects of adding scavengers on the photocatalytic efficiency of CR solution on $NiFe_2O_4$/ZnO hybrids.

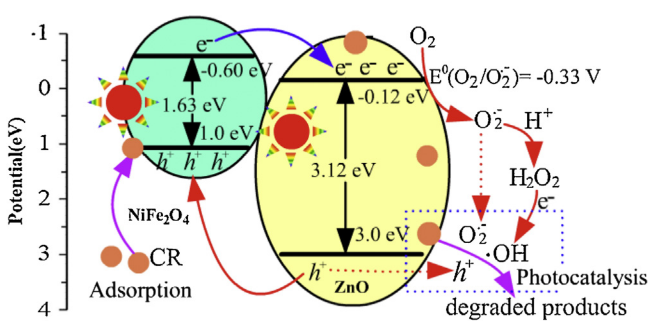

Fig. 9. Proposed mechanism diagram of the CR dyes removal over $NiFe_2O_4$/ZnO hybrids.

proposed photocatalytic mechanism of $NiFe_2O_4$/ZnO hybrids was presumed (Fig. 9). At first, CR moleculars in aqueous solution are adsorbed on $NiFe_2O_4$/ZnO hybrids [34] (Eq. (7)), which leads to dye-sensitization of ZnO in $NiFe_2O_4$/ZnO hybrids [53]. Under simulated solar light irradiation, electrons (e^-) in the valence band (VB) of dye-sensitized ZnO and $NiFe_2O_4$ will be excited to the CB while the same amount of holes (h^+) in the VB (Eq. (8)). The CB potential of ZnO is more positive than that of the $NiFe_2O_4$ while the VB potential of $NiFe_2O_4$ is more negative than that of the ZnO [9,29]. Therefore, the photoelectrons (e^-) photoproduced in $NieFe_2O_4$ were transferred across the interface of the $NiFe_2O_4$/ZnO hybrids to the surface of ZnO (Eq. (9)). At the same time, some holes (h^+) are transferred injected quickly from ZnO to $NiFe_2O_4$ due to the more negative VB potential of $NiFe_2O_4$ than that of the ZnO and the close interphase contact of $NiFe_2O_4$ and ZnO. The fast migration of h^+ and e^- lead to the improved lifetime and transfer of photo-generated charge carriers [41]. The dissolved oxygen (O_2) in aqueous solution acting as the electron scavenger react with electrons to yield active free radicals (${}^\bullet OH$, $O_2{}^{\bullet -}$, etc.) (Eqs. (10) and (11)). The separated holes will react with electron donors (H_2O) to yield active ${}^\bullet OH$ free radicals (Eq. (12)). Subsequently, the surface-adsorbed CR molecules were attacked by the generated h^+ and other free radicals (${}^\bullet OH$, $O_2{}^{\bullet -}$, etc.), leading to the decolorization and opening-ring reactions (Eq. (13)).

$$\text{CR (in aqueous solution)} + NiFe_2O_4/ZnO \rightarrow \text{CR-}NiFe_2O_4/ZnO \quad (7)$$

$$\text{CR-}NiFe_2O_4/ZnO + h\nu \rightarrow \text{CR-}NiFe_2O_4(h^+ + e^-)/ZnO(h^+ + e^-) \quad (8)$$

$$\text{CR-}NiFe_2O_4(h^+ + e^-)/ZnO(h^+ + e^-) \rightarrow \text{CR-}NiFe_2O_4(h^+)/ZnO(e^-) \quad (9)$$

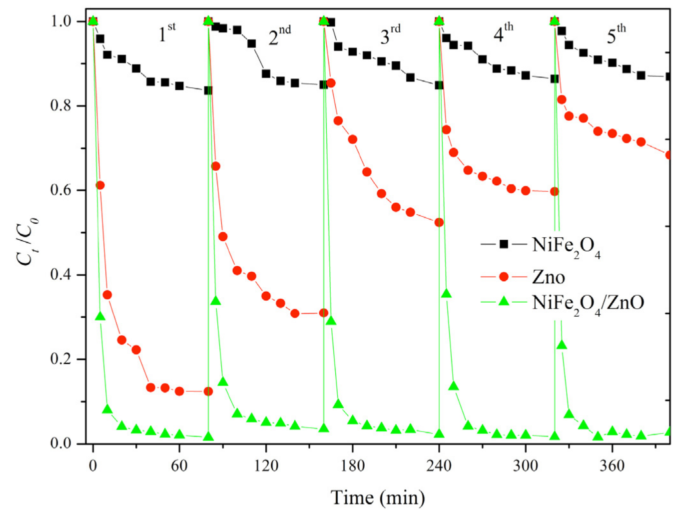

Fig. 10. 5 recycling experiments of ZnO, $NiFe_2O_4$ and $NiFe_2O_4$/ZnO hybrids for CR decolorization (initial CR concentration: 20 mg L^{-1}; dosage: 1.0 g L^{-1}; natural pH).

$$e^- + O_2 \rightarrow O_2{}^{\bullet -} \quad (10)$$

$$O_2{}^{\bullet -} + H^+ + e^- \rightarrow {}^\bullet OH + OH^- \quad (11)$$

$$h^+ + H_2O \rightarrow {}^\bullet OH + H^+ \quad (12)$$

$$\text{CR-}NiFe_2O_4/ZnO + h^+/{}^\bullet OH/O_2{}^{\bullet -} \rightarrow NiFe_2O_4/ZnO + CO_2 + H_2O + \text{other byproducts} \quad (13)$$

3.4. Recyclability and photostability of $NiFe_2O_4$/ZnO for decolorization of CR solution

From the view of economical large scale practical application, the long-term reuse of materials is quite significant [16]. To evaluate the photostability and reusability of $NiFe_2O_4$/ZnO, five successive recycling tests for decolorization of CR solution have been performed under simulated solar light irradiation, as shown in Fig. 10. For further use, the used ZnO nanoparticles were recovered by centrifugation while $NiFe_2O_4$ and $NiFe_2O_4$/ZnO by magnetic separation. Then those materials were washed with distilled water, and finally dried at 105 °C. As can be seen in Fig. 10, the decolorization efficiency of CR solution by ZnO nanoparticles for the first cycle is 87.44% after 80 min irradiation while it is reduced to 32.03% for the fifth cycle. The obvious decrease in the photocatalytic activity of ZnO can be due to the loss of ZnO during the washing and filtration procedure [18] and the serious photocorrosion under light irradiation [17]. As for $NiFe_2O_4$, no significant loss of photocatalytic activity is observed after the fifth-cycle process. However, the decolorization of CR solution by $NiFe_2O_4$ is too low to meet the need of practical application. The photocatalytic decolorization of CR solution by $NiFe_2O_4$/ZnO hybrids is 98.43% and 97.23% during the first and fifth cycles, respectively. The photocatalytic efficiency of $NiFe_2O_4$/ZnO hybrids for removing CR solution does not reduce even after five runs since magnetic separation can effectively prevent the loss of the nanomaterials during recovery [7,41]. In addition, the close interphase coupling of $NiFe_2O_4$ and ZnO nanoparticles in $NiFe_2O_4$/ZnO hybrids may play an important role in enhancing the photostability. The fact that the decolorization rate of CR solution is over 97% for fifth times indicate that the prepared $NiFe_2O_4$/ZnO hybrids should further be an ideal material for the long term application in the treatment of CR solution wastewater.

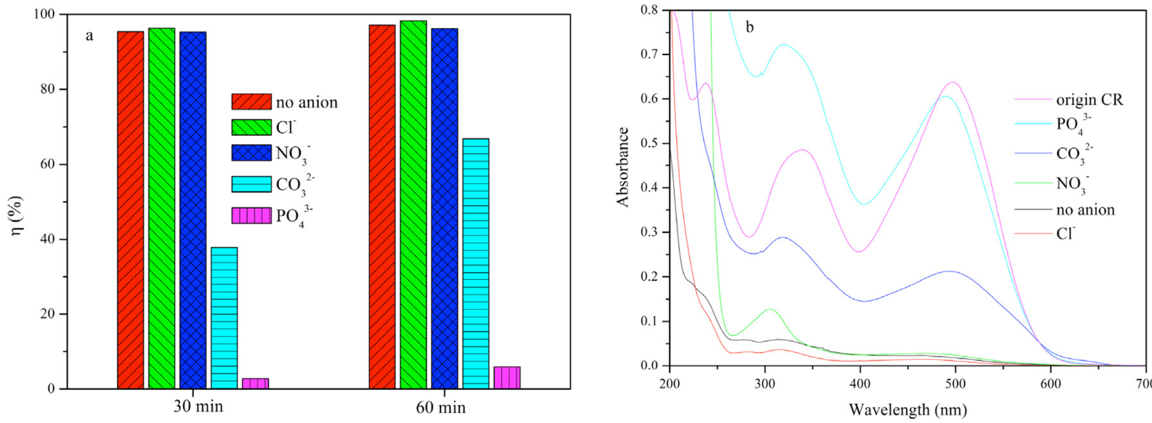

Fig. 11. Effect of co-existing anions on the CR decolorization by $NiFe_2O_4$/ZnO hybrids and UV–vis absorption spectra of CR solution (initial CR concentration: 20 mg L^{-1}; dosage: 1.0 g L^{-1}).

3.5. Effect of inorganic anions on decolorization of CR solution by $NiFe_2O_4$/ZnO hybrids

In practical dye-containing industrial wastewater, various electrolytes (such as NO_3^-, Cl^-) are often added into the dye bath in the textile industries in order to retard dyeing rates and improve color fastness [54]. Therefore, the impact of ubiquitous anions on photocatalytic decolorization of CR solution by $NiFe_2O_4$/ZnO hybrids was investigated using corresponding sodium salts since Na^+ will not compete as a hole scavenger because of its maximum oxidation state [55]. As can be seen in Fig. 11a, both NO_3^- and Cl^- do not influence the decolorization rates by $NiFe_2O_4$/ZnO hybrids, while PO_4^{3-} and CO_3^{2-} anions are found to decrease obviously the decolorization efficiency of CR solution. The inhibitory effect of PO_4^{3-} and CO_3^{2-} on the decolorization of CR is attributed to the formation of less active inorganic radical species and competitive adsorption [56]. In the presence of different anions, the absorbance of the CR solution at 270.1 nm is in the following decreasing order: $PO_4^{3-} > CO_3^{2-} > NO_3^- >$ no anion addition > Cl^- (Fig. 10b), indicating that the presence of Cl^- anions would be a somehow acceleration of opening benzene ring of CR dyes by $NiFe_2O_4$/ZnO hybrids. In a word, NO_3^- and Cl^- which are all ubiquitous components in dye-containing wastewater have negligible influence on the effectiveness of $NiFe_2O_4$/ZnO.

4. Conclusions

Novel multifunctional $NiFe_2O_4$/ZnO hybrids were fabricated by a hydrothermal method. $NiFe_2O_4$/ZnO hybrids exhibit comparable adsorption capacities and photoactivity than ZnO, $NiFe_2O_4$ and m-$NiFe_2O_4$/ZnO for decolorization of CR solution under simulated solar light irradiation. $NiFe_2O_4$/ZnO hybrids can be quickly separated from aqueous solution because of its high saturation magnetization, low remanence, and small coercivity. $NiFe_2O_4$/ZnO hybrids show higher photocatalytic activity than that of ZnO nanoparticles and maintained excellent photocatalytic activity and photostability after five cycles. •OH and photoproduced holes h^+ are main species in removal of CR solution by $NiFe_2O_4$/ZnO hybrids. NO_3^- and Cl^- which are all ubiquitous components in dye-containing wastewater have no influence on the effectiveness of $NiFe_2O_4$/ZnO hybrids. As a result, novel multifunctional $NiFe_2O_4$/ZnO hybrids with the combined properties of high adsorption, excellent photocatalytic activity and magnetically separation may greatly promote the potential applications in eliminating organic pollutants.

Acknowledgments

Financial support for this research was provided by the Natural Science Foundation of Zhejiang Province, China (Grant No. LY14B070011 and LY15E080002) and the Natural Science Foundation of China (Grant No. 51208331, 21007044) and Special Funds of Innovative Research Team on Plant Evolutionary Ecology.

References

[1] A. Akhundi, A. Habibi-Yangjeh, Ternary g-C_3N_4/ZnO/AgCl nanocomposites: synergistic collaboration on visible-light-driven activity in photodegradation of an organic pollutant, Appl. Surf. Sci. 358 (2015) 261–269.
[2] R. Jiang, H.Y. Zhu, J.B. Li, F.Q. Fu, J. Yao, S.T. Jiang, G.M. Zeng, Fabrication of novel magnetically separable BiOBr/$CoFe_2O_4$ microspheres and its application in the efficient removal of dye from aqueous phase by an environment-friendly and economical approach, Appl. Surf. Sci. 364 (2016) 604–612.
[3] S.G. Kumar, K.S.R.K. Rao, Zinc oxide based photocatalysis: tailoring surface bulk structure and related interfacial charge carrier dynamics for better environmental applications, RSC Adv. 5 (2015) 3306–3351.
[4] S.M. Lam, J.C. Sin, A.Z. Abdullah, A.R. Mohamed, Degradation of wastewaters containing organic dyes photocatalysed by zinc oxide: a review, Desalin. Water Treat. 41 (2012) 131–169.
[5] J. Low, J. Yu, Q. Li, B. Cheng, Enhanced visible-light photocatalytic activity of plasmonic Ag and graphene co-modified Bi_2WO_6 nanosheets, Phys. Chem. Chem. Phys. 16 (2014) 1111–1120.
[6] D. Xu, B. Cheng, S. Cao, J. Yu, Enhanced photocatalytic activity and stability of Z-scheme Ag_2CrO_4-GO composite photocatalysts for organic pollutant degradation, Appl. Catal. B: Environ. 164 (2015) 380–388.
[7] Y. Wang, J. Ning, E. Hu, C. Zheng, Y. Zhong, Y. Hu, Direct coating ZnO nanocrystals onto 1D Fe_3O_4/C composite microrods as highly efficient and reusable photocatalysts for water treatment, J. Alloys Compd. 637 (2015) 301–307.
[8] Y. Liu, R. Wang, Z. Yang, H. Du, Y. Jiang, C. Shen, Enhanced visible-light photocatalytic activity of Z-scheme graphitic carbon nitride/oxygen vacancy-rich zinc oxide hybrid photocatalysts, Chin. J. Catal. 36 (2015) 2135–2144.
[9] K.K. Chattopadhyay, S. Maiti, S. Pal, Recent advances in low temperature, solution processed morphology tailored ZnO nano-architecture for electron emission and photocatalysis applications, CrystEngComm 17 (2015) 9264–9295.
[10] Y. Chen, C. Zhang, W. Huang, Y. Situ, H. Huang, Multimorphologies nano-ZnO preparing through a simple solvothermal method for photocatalytic application, Mater. Lett. 141 (2015) 294–297.
[11] J.C. Colmenares, E. Kuna, S. Jakubiak, J. Michalski, K. Kurzydłowski, Polypropylene nonwoven filter with nanosized ZnO rods: promising hybrid photocatalyst for water purification, Appl. Catal. B: Environ. 170–171 (2015) 273–282.
[12] K.M. Lee, C.W. Lai, K.S. Ngai, J.C. Juan, Recent developments of zinc oxide based photocatalyst in water treatment technology: a review, Water Res. 88 (2016) 428–448.
[13] Y. Liu, L. Sun, J. Wu, T. Fang, R. Cai, A. Wei, Preparation and photocatalytic activity of ZnO/Fe_2O_3 nanotube composites, Mater. Sci. Eng. B 194 (2015) 9–13.
[14] M.J. Sampaio, R.R. Bacsa, A. Benyounes, R. Axet, P. Serp, C.G. Silva, A.M.T. Silva, J.L. Faria, Synergistic effect between carbon nanomaterials and ZnO for photocatalytic water decontamination, J. Catal. 331 (2015) 172–180.

[15] M. Sun, T. Li, Z. Zhang, N. Wang, A. Xie, X. Lv, Y. Wang, F. Wu, M. Wang, Natural biological template for ZnO nanoparticle growth and photocatalytic dye degradation under visible light, RSC Adv. 5 (2015) 84406–84409.
[16] Y. Li, K. Wang, J. Wu, L. Gu, Z. Lu, X. Wang, X. Cao, Synthesis of highly permeable Fe_2O_3/ZnO hollow spheres for printable photocatalysis, RSC Adv. 5 (2015) 88277–88286.
[17] C. Han, M.Q. Yang, B. Weng, Y.J. Xu, Improving the photocatalytic activity and anti-photocorrosion of semiconductor ZnO by coupling with versatile carbon, Phys. Chem. Chem. Phys. 16 (2014) 16891–16903.
[18] D. Tang, H. Ye, D. Du, S. Liu, M. Li, X. Wu, L. Wen, K. Lv, K. Deng, Fabrication of ZnO/graphene flake-like photocatalyst with enhanced photoreactivity, Appl. Surf. Sci. 358 (2015) 130–136.
[19] J.K. Vaishnav, S.S. Arbuj, S.B. Rane, D.P. Amalnerkar, One dimensional CdS/ZnO nanocomposites: an efficient photocatalyst for hydrogen generation, RSC Adv. 4 (2014) 47637–47642.
[20] H.Y. Zhu, L. Xiao, R. Jiang, G.M. Zeng, L. Liu, Efficient decolorization of azo dye solution by visible light-induced photocatalytic process using SnO_2/ZnO heterojunction immobilized in chitosan matrix, Chem. Eng. J. 172 (2011) 746–753.
[21] H. Zhu, R. Jiang, Y. Fu, Y. Guan, J. Yao, L. Xiao, G. Zeng, Effective photocatalytic decolorization of methyl orange utilizing TiO_2/ZnO/chitosan nanocomposite films under simulated solar irradiation, Desalination 286 (2012) 41–48.
[22] T. Xin, M. Ma, H. Zhang, J. Gu, S. Wang, M. Liu, Q. Zhang, A facile approach for the synthesis of magnetic separable Fe_3O_4@TiO_2 core–shell nanocomposites as highly recyclable photocatalysts, Appl. Surf. Sci. 288 (2014) 51–59.
[23] G. Shan, Y. Fu, X. Chu, C. Chang, L. Zhu, Highly active magnetic bismuth tungstate/magnetite composite under visible light irradiation in the presence of hydrogen peroxide, J. Colloid Interface Sci. 444 (2015) 123–131.
[24] Y. Liu, L. Yu, Y. Hu, C. Guo, F. Zhang, X. Wen David Lou, A magnetically separable photocatalyst based on nest-like γ-Fe_2O_3/ZnO double-shelled hollow structures with enhanced photocatalytic activity, Nanoscale 4 (2012) 183–187.
[25] J. Li, Z. Liu, Z. Zhu, Enhanced photocatalytic activity in $ZnFe_2O_4$–ZnO–Ag_3PO_4 hollow nanospheres through the cascadal electron transfer with magnetical separation, J. Alloys Compd. 636 (2015) 229–233.
[26] X. Guo, H. Zhu, Q. Li, Visible-light-driven photocatalytic properties of ZnO/$ZnFe_2O_4$ core/shell nanocable arrays, Appl. Catal. B: Environ. 160–161 (2014) 408–414.
[27] H.Y. Zhu, R. Jiang, S.H. Huang, J. Yao, F.Q. Fu, J.B. Li, Novel magnetic $NiFe_2O_4$/multi-walled carbon nanotubes hybrids: facile synthesis, characterization, and application to the treatment of dyeing wastewater, Ceram. Int. 41 (2015) 11625–11631.
[28] P. Sathishkumar, N. Pugazhenthiran, R.V. Mangalaraja, A.M. Asiri, S. Anandan, ZnO supported $CoFe_2O_4$ nanophotocatalysts for the mineralization of Direct Blue 71 in aqueous environments, J. Hazard. Mater. 252–253 (2013) 171–179.
[29] A. Ren, C. Liu, Y. Hong, W. Shi, S. Lin, P. Li, Enhanced visible-light-driven photocatalytic activity for antibiotic degradation using magnetic $NiFe_2O_4$/Bi_2O_3 heterostructures, Chem. Eng. J. 258 (2014) 301–308.
[30] K.C. Verma, V.P. Singh, M. Ram, J. Shah, R.K. Kotnala, Structural, microstructural and magnetic properties of $NiFe_2O_4$, $CoFe_2O_4$ and $MnFe_2O_4$ nanoferrite thin films, J. Magn. Magn. Mater. 323 (2011) 3271–3275.
[31] P. Sivakumar, R. Ramesh, A. Ramanand, S. Ponnusamy, C. Muthamizhchelvan, Preparation of sheet like polycrystalline $NiFe_2O_4$ nanostructure with PVA matrices and their properties, Mater. Lett. 65 (2011) 1438–1440.
[32] T. Peng, X. Zhang, H. Lv, L. Zan, Preparation of $NiFe_2O_4$ nanoparticles and its visible-light-driven photoactivity for hydrogen production, Catal. Commun. 28 (2012) 116–119.
[33] S.V. Bhosale, N.S. Kanhe, S.V. Bhoraskar, S.K. Bhat, R.N. Bulakhe, J.J. Shim, V.L. Mathe, Micro-structural analysis of $NiFe_2O_4$ nanoparticles synthesized by thermal plasma route and its suitability for BSA adsorption, J. Mater. Sci.: Mater. Med. 26 (2015) 216–230.
[34] X. Hou, J. Feng, X. Liu, Y. Ren, Z. Fan, T. Wei, J. Meng, M. Zhang, Synthesis of 3D porous ferromagnetic $NiFe_2O_4$ and using as novel adsorbent to treat wastewater, J. Colloid Interface Sci. 362 (2011) 477–485.
[35] P. Xiong, Y. Fu, L. Wang, X. Wang, Multi-walled carbon nanotubes supported nickel ferrite: a magnetically recyclable photocatalyst with high photocatalytic activity on degradation of phenols, Chem. Eng. J. 195–196 (2012) 149–157.
[36] J. Jiang, L.H. Ai, L.C. Li, H. Liu, Facile fabrication and characterization of $NiFe_2O_4$/ZnO hybrid nanoparticles, J. Alloys Compd. 484 (2009) 69–72.
[37] Y. Khan, S.K. Durrani, M. Mehmood, J. Ahmad, M.R. Khan, S. Firdous, Low temperature synthesis of fluorescent ZnO nanoparticles, Appl. Surf. Sci. 257 (2010) 1756–1761.
[38] P.V. Kumar, M.P. Short, S. Yip, B. Yildiz, J.C. Grossman, High surface reactivity and water adsorption on $NiFe_2O_4$ (111) surfaces, J. Phys. Chem. C 117 (2013) 5678–5683.
[39] A. Xia, S. Ren, C. Zuo, L. Zhang, M. Xie, Y. Deng, R. Wu, W. Xu, C. Jin, X. Liu, Facile hydrothermal synthesis of core/shell-like composite $SrFe_{12}O_{19}$/(Ni, Zn)Fe_2O_4 nanopowders and their magnetic properties, RSC Adv. 4 (2014) 18885–18888.
[40] M. Kruk, M. Jaronies, Gas adsorption characterization of ordered organic-inorganic nanocomposite materials, Chem. Mater. 13 (2001) 3169–3183.
[41] Y. Yao, J. Qin, H. Chen, F. Wei, X. Liu, J. Wang, S. Wang, One-pot approach for synthesis of N-doped TiO_2/$ZnFe_2O_4$ hybrid as an efficient photocatalyst for degradation of aqueous organic pollutants, J. Hazard. Mater. 291 (2015) 28–37.
[42] B. Zhang, J. Zhang, F. Chen, Preparation and characterization of magnetic TiO_2/$ZnFe_2O_4$ photocatalysts by a sol–gel method, Res. Chem. Intermed. 34 (2008) 375–380.
[43] C. Karunakaran, P. Vinayagamoorthy, J. Jayabharathi, Nonquenching of charge carriers by Fe_3O_4 core in Fe_3O_4/ZnO nanosheet photocatalyst, Langmuir 30 (2014) 15031–15039.
[44] Q. He, Z. Zhang, J. Xiong, Y. Xiong, H. Xiao, A novel biomaterial — Fe_3O_4:TiO_2 core-shell nano particle with magnetic performance and high visible light photocatalytic activity, Opt. Mater. 31 (2008) 380–384.
[45] H.M.F. Freundlich, Over the adsorption in solution, Z. Phys. Chem. A 57 (1906) 358–471.
[46] I. Langumuir, The adsorption of gases on plane surfaces of glass, mica, and platinum, J. Am. Chem. Soc. 40 (1918) 1361–1403.
[47] S. Liu, S. Kang, G. Wang, H. Zhao, W. Cai, Micro/nanostructured porous Fe–Ni binary oxide and its enhanced arsenic adsorption performances, J. Colloid Interface Sci. 458 (2015) 94–102.
[48] B. Cheng, Y. Le, W. Cai, J. Yu, Synthesis of hierarchical $Ni(OH)_2$ and NiO nanosheets and their adsorption kinetics and isotherms to congo red in water, J. Hazard. Mater. 185 (2011) 889–897.
[49] L. Wang, J. Li, Y. Wang, L. Zhao, Preparation of nanocrystalline $Fe_{3-x}La_xO_4$ ferrite and their adsorption capability for congo red, J. Hazard. Mater. 196 (2011) 342–349.
[50] A. Afkhami, R. Moosavi, Adsorptive removal of congo red, a carcinogenic textile dye, from aqueous solutions by maghemite nanoparticles, J. Hazard. Mater. 174 (2010) 398–403.
[51] R. Rahimi, H. Kerdari, M. Rabbani, M. Shafiee, Synthesis, characterization and adsorbing properties of hollow Zn-Fe_2O_4 nanospheres on removal of congo red from aqueous solution, Desalination 280 (2011) 412–418.
[52] L. Wang, J. Li, Y. Wang, L. Zhao, Q. Jiang, Adsorption capability for congo red on nanocrystalline MFe_2O_4 (M = Mn, Fe, Co, Ni) spinel ferrites, Chem. Eng. J. 181–182 (2012) 72–79.
[53] J.J. Wu, G.R. Chen, H.H. Yang, C.H. Ku, J.Y. Lai, Effects of dye adsorption on the electron transport properties in ZnO-nanowire dye-sensitized solar cells, Appl. Phys. Lett. 90 (2007) 213109.
[54] R. Jiang, Y. Guan, H. Zhu, Y. Fu, Effect of inorganic anions on the photocatalytic decolorisation of an azo dye in the aqueous phase by cadmium sulphide/polymer nanocomposite films under visible light irradiation, Color. Technol. 127 (2011) 426–433.
[55] D. Wang, Y. Li, G. Li, C. Wang, W. Zhang, Q. Wang, Modeling of quantitative effects of water components on the photocatalytic degradation of 17α-ethynylestradiol in a modified flat plate serpentine reactor, J. Hazard. Mater. 254–255 (2013) 64–71.
[56] L.G. Devi, K.S.A. Raju, S.G. Kumar, K.E. Rajashekhar, Photo-degradation of di azo dye Bismarck Brown by advanced photo-Fenton process: influence of inorganic anions and evaluation of recycling efficiency of iron powder, J. Taiwan Inst. Chem. Eng. 42 (2011) 341–349.